Infrared electromagnetic field detected by a dipolar tip above a material

Karl Joulain, Philippe Ben-Abdallah, Pierre-Olivier Chapuis, Arthur Babuty, Yannick de Wilde

Infrared electromagnetic field detected by a dipolar tip above a material

Karl Joulain

Institut PPrime, CNRS-Université de Poitiers,

UPR 3346, 2, Rue Pierre Brousse,

B.P 633, 86022 Poitiers Cedex, France.

P. Ben-Abdallah

Laboratoire Charles Fabry, UMR 8501,

Institut d'Optique, CNRS, Université Paris-Sud 11,

2 avenue Augustin Fresnel, 91127 Palaiseau Cedex, France

P.-O. Chapuis

CETHIL, CNRS-INSA Lyon, UMR 5008,

9 rue de la physique, 69621 Villleurbanne Cedex, France

Y. De Wilde and A. Babuty

Institut Langevin, ESPCI Paris Tech,

10 rue Vauquelin, 75005 Paris, France

(Dated: Monday, January 23rd 2012)

Abstract

We show in this article how an electric and magnetic dipolar particle has its polarisability that is changed in a non-vacuum environment. This result is used to calculate the signal obtained by an apertureless Scanning Near-Field Optical Microscope (SNOM) when the tip is a dipolar particle. This signal only depends on the field without tip and on the particle and surface optical properties. We apply our theory results to the case where the surface excited by a polariton and to the case where it is thermally excited. In this last situation we show that the measure obtained is a local surface spectroscopy. We specify the practical situations where the signal detected by the SNOM can be related to the electromagnetic Local Density of States (LDOS). We finally examine the cooling rate of a dipolar particle is modified when the particle is approached to a surface and how a heated particle can be used to make a local spectroscopy

PACS numbers: 44.40.+a,05.40-a,78.67.Pt

I. INTRODUCTION

Since the seminal works of Rytov[3], it is known that heat radiation has a different behaviour when the caracteristic lengths involved are large or small compared to the thermal wavelength[4–6]. For example heat transfer at subwavelength distance can exceed by far the one between perfect blackbodies[7]. Energy density[8] and coherence properties[9] are also greatly affected in the near-field, especially close to materials exhibiting resonances such as polaritons. Knowing precisely how the electromagnetic field behaves close to a surface is therefore an important issue in order to address all potential applications of near-field heat transfer.

From an experimental point of view, near-field radiation coherence properties have been operated to produce directional and monochromatic thermal sources[10–12]. Near-field radiative heat transfer enhancement have been detected more recently by means of probe microscopy techniques[13–16]. Near-field thermal imaging has also been used in scanning near-field optical microscopy (SNOM) in order to image surface without external enlightment[17,18]. These experimental techniques all use a small probe put close to a material surface studied. When the probe is approached near the surface, mutual interaction between the tip and the surface modifies the local field and probe optical properties such as its polarisability. This makes the signal scattered by the tip and detected in the far-field complicated by multiple interactions between the bodies involved[19–22] although one can relate this signal to the surface material optical properties. In particular, a question that has been asked for a while now is to know how the near-field thermal signal scattered by a tip and detected in the far-field can be related to the electromagnetic local density of states (LDOS)[23,24]. Is there a way that a SNOM detecting thermal radiation might be the electromagnetic equivalent of the scanning tunneling microscope detecting electronic LDOS[25]. Moreover, when a probe is heated, one can wonder how fast it cools down or what is the signal detected in far-field when it is approached close to a surface.

If some of these questions have already been addressed in the past[23,26], our goal is here to clarify these interrogations. We will first see, following previous similar works how the particle polarisability is modified by multiple interactions with the surface. Then, we will use this theory to calculate the signal detected in far-field due to the scattering of a near-field signal by a dipolar probe. We will illustrate this theory with the study of the SNOM signal obtained close to a surface excited by a plasmon and next in the general case of near-field

thermal emission. We will consider in the following two parts a dipolar tip heated above a sample. We will show first how heat cooling is increased as the particle is approached close to the surface. We will finish by giving the signal detected in far field coming from a heated dipolar probe and reflected by the surface considered.

II. EFFECTIVE POLARISABILITY

A. Introduction

We propose here to calculate the polarisability of dipolar particle when this particle is placed in an environment different from vacuum. The idea is the following. When a dipolar particle is situated in a system, the electromagnetic field present in the system enlights the particle and creates a dipole at the particle position. This dipole radiates a field everywhere in space including at the particle position. These interactions between the dipole induced by the particle and the field in the system modify particle polarisability (Fig. 1).

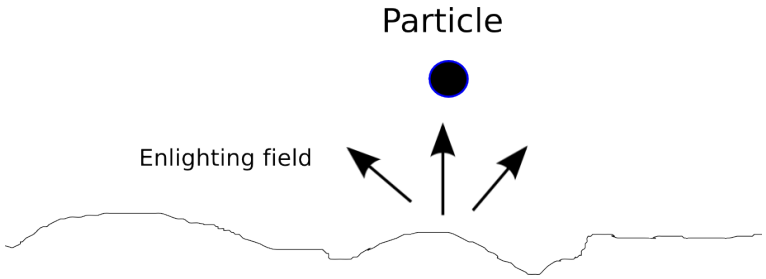

FIG. 1. System scheme

B. Calculation of effective polarisability

Let us call $\mathbf{E}^0$ the electromagnetic field in the system in the absence of particle. When a particle is placed in the system, an electric dipole $\mathbf{p}$ and a magnetic dipole $\mathbf{m}$ will appear at the position of the particle $\mathbf{r}_p$. These dipoles radiate a field : the total local field $\mathbf{E}^{loc}$ is the sum of the field in the absence of particle with the field radiated by the dipoles. In the following, we write the dipole radiated field with the Green's tensor help.

$$\mathbf{E}^{loc}(\mathbf{r}) = \mathbf{E}^0(\mathbf{r}) + \overleftrightarrow{\mathbf{G}}^{EE}(\mathbf{r}, \mathbf{r}_p) \cdot \mathbf{p} + \overleftrightarrow{\mathbf{G}}^{EH}(\mathbf{r}, \mathbf{r}_p) \cdot \mathbf{m} \tag{1}$$

that can also be written

$$\mathbf{E}^{loc}(\mathbf{r}) = \mathbf{E}^0(\mathbf{r}) + \overset{\leftrightarrow}{\mathbf{G}}^{EE}(\mathbf{r},\mathbf{r}_p)\cdot\alpha^E\mathbf{E}^{loc}(\mathbf{r}_p) + \overset{\leftrightarrow}{\mathbf{G}}^{EH}(\mathbf{r},\mathbf{r}_p)\cdot\alpha^H\mathbf{H}^{loc}(\mathbf{r}_p) \tag{2}$$

where α^E and α^H are the particle electric and magnetic dipoles when it is alone in vacuum.

Analogous expressions exist for the magnetic field

$$\mathbf{H}^{loc}(\mathbf{r}) = \mathbf{H}^0(\mathbf{r}) + \overset{\leftrightarrow}{\mathbf{G}}^{HE}(\mathbf{r},\mathbf{r}_p)\cdot\mathbf{p} + \overset{\leftrightarrow}{\mathbf{G}}^{HH}(\mathbf{r},\mathbf{r}_t)\cdot\mathbf{m} \tag{3}$$

that can also be written

$$\mathbf{H}^{loc}(\mathbf{r}) = \mathbf{H}^0(\mathbf{r}) + \overset{\leftrightarrow}{\mathbf{G}}^{HE}(\mathbf{r},\mathbf{r}_p)\cdot\alpha^E\mathbf{E}_{loc}(\mathbf{r}_p) + \overset{\leftrightarrow}{\mathbf{G}}^{HH}(\mathbf{r},\mathbf{r}_p)\cdot\alpha^H\mathbf{H}^{loc}(\mathbf{r}_p) \tag{4}$$

The Green tensors used here are of four type : $\overset{\leftrightarrow}{\mathbf{G}}^{EE}(\mathbf{r},\mathbf{r}_p)$ is the Green tensor that give the electric field at position $\mathbf{r}$ when an electric dipole is placed at $\mathbf{r}_p$. In the same way, $\overset{\leftrightarrow}{\mathbf{G}}^{EH}(\mathbf{r},\mathbf{r}_p)$ is the Green tensor that give the electric field at position $\mathbf{r}$ when an magnetic dipole is placed at $\mathbf{r}_p$. $\overset{\leftrightarrow}{\mathbf{G}}^{HE}$ and $\overset{\leftrightarrow}{\mathbf{G}}^{HH}$ respectively gives the magnetic field of an electric and a magnetic dipole. These Green tensors, which can all be expressed in terms of $\overset{\leftrightarrow}{\mathbf{G}}^{EE}(\mathbf{r},\mathbf{r}_p)$[27], are the sum of a direct contribution (that is the Green tensor in vacuum) and of a perturbed contribution. When one considers the electromagnetic field at the particle position $\mathbf{r}_p$, only the perturbed Green tensor contributes. Then, the local field is obtained solving the system (2) (4).

$$\mathbf{E}^{loc}(\mathbf{r}_p) = \overset{\leftrightarrow}{\mathbf{A}}^{-1}\mathbf{E}^0(\mathbf{r}_p) + \overset{\leftrightarrow}{\mathbf{B}}^{-1}\mathbf{H}^0(\mathbf{r}_p) \tag{5}$$

$$\mathbf{H}^{loc}(\mathbf{r}_t) = \overset{\leftrightarrow}{\mathbf{C}}^{-1}\mathbf{E}^0(\mathbf{r}_p) + \overset{\leftrightarrow}{\mathbf{D}}^{-1}\mathbf{H}^0(\mathbf{r}_p) \tag{6}$$

where

$$\overset{\leftrightarrow}{\mathbf{A}} = [\overset{\leftrightarrow}{\mathbf{I}} - \alpha^E\overset{\leftrightarrow}{\mathbf{G}}^{EE}(\mathbf{r}_p,\mathbf{r}_p)] - \alpha^H\overset{\leftrightarrow}{\mathbf{G}}^{EH}(\mathbf{r}_p,\mathbf{r}_p)[\overset{\leftrightarrow}{\mathbf{I}} - \alpha^H\overset{\leftrightarrow}{\mathbf{G}}^{HH}(\mathbf{r}_p,\mathbf{r}_p)]^{-1}\alpha^E\overset{\leftrightarrow}{\mathbf{G}}^{HE}(\mathbf{r}_p,\mathbf{r}_p) \tag{7}$$

$$\overset{\leftrightarrow}{\mathbf{B}} = -\alpha^E\overset{\leftrightarrow}{\mathbf{G}}^{HE}(\mathbf{r}_p,\mathbf{r}_p) + [\overset{\leftrightarrow}{\mathbf{I}} - \alpha^H\overset{\leftrightarrow}{\mathbf{G}}^{HH}(\mathbf{r}_p,\mathbf{r}_p)][\alpha^H\overset{\leftrightarrow}{\mathbf{G}}^{EH}(\mathbf{r}_p,\mathbf{r}_p)]^{-1}[\overset{\leftrightarrow}{\mathbf{I}} - \alpha^E\overset{\leftrightarrow}{\mathbf{G}}^{EE}(\mathbf{r}_p,\mathbf{r}_p)] \tag{8}$$

$$\overset{\leftrightarrow}{\mathbf{C}} = -\alpha^H\overset{\leftrightarrow}{\mathbf{G}}^{EH}(\mathbf{r}_p,\mathbf{r}_p) + [\overset{\leftrightarrow}{\mathbf{I}} - \alpha^E\overset{\leftrightarrow}{\mathbf{G}}^{EE}(\mathbf{r}_p,\mathbf{r}_p)][\alpha^E\overset{\leftrightarrow}{\mathbf{G}}^{HE}(\mathbf{r}_p,\mathbf{r}_p)]^{-1}[\overset{\leftrightarrow}{\mathbf{I}} - \alpha^H\overset{\leftrightarrow}{\mathbf{G}}^{HH}(\mathbf{r}_p,\mathbf{r}_p)] \tag{9}$$

$$\overset{\leftrightarrow}{\mathbf{D}} = [\overset{\leftrightarrow}{\mathbf{I}} - \alpha^H\overset{\leftrightarrow}{\mathbf{G}}^{HH}(\mathbf{r}_p,\mathbf{r}_p)] - \alpha^E\overset{\leftrightarrow}{\mathbf{G}}^{HE}(\mathbf{r}_p,\mathbf{r}_p)[\overset{\leftrightarrow}{\mathbf{I}} - \alpha^E\overset{\leftrightarrow}{\mathbf{G}}^{EE}(\mathbf{r}_p,\mathbf{r}_p)]^{-1}\alpha^H\overset{\leftrightarrow}{\mathbf{G}}^{EH}(\mathbf{r}_p,\mathbf{r}_p) \tag{10}$$

The preceding equations are general for the calculation of a local field at dipole position. Apart from the fact that magnetic dipole is taken into account, the self-consistent reasoning

used to obtain local fields is very similar to previous work using the so-called coupled dipole theory such as[19,20,28,29]. Local fields only depend on the system Green tensors. Particle dipoles can be related to the field at the tip position in the absence of particle

$$\begin{pmatrix} \mathbf{p} \\ \mathbf{m} \end{pmatrix} = \begin{pmatrix} \alpha^E \overleftrightarrow{\mathbf{A}} & \alpha^H \overleftrightarrow{\mathbf{B}} \\ \alpha^E \overleftrightarrow{\mathbf{C}} & \alpha^H \overleftrightarrow{\mathbf{D}} \end{pmatrix} \begin{pmatrix} \mathbf{E}^0 \\ \mathbf{H}^0 \end{pmatrix} \tag{11}$$

so that the four elements in the matrix can be seen as effective polarisability expressions.

We now go to the case of a simple system constituted of a plane interface separating a material from vacuum. In this situation, Green tensors are well known[27,30] and can be written knowing the materials optical properties. Let us begin by the direct Green tensors

$$\overleftrightarrow{\mathbf{G}}_0^{AB}(\mathbf{r},\mathbf{r}',\omega) = \frac{ik_0^2 C_{AB}}{8\pi^2}\int \frac{d^2\mathbf{K}}{\gamma}(e_A^{\hat{s}-}e_B^{\hat{s}-} + e_A^{\hat{p}-}e_B^{\hat{p}-})e^{i\mathbf{K}.(\mathbf{R}-\mathbf{R}')}e^{-i\gamma(z-z')} \tag{12}$$

Concerning the reflected field

$$\overleftrightarrow{\mathbf{G}}_R^{AB}(\mathbf{r},\mathbf{r}',\omega) = \frac{ik_0^2 C_{AB}}{8\pi^2}\int \frac{d^2\mathbf{K}}{\gamma}(e_A^{\hat{s}+}r^s e_B^{\hat{s}-} + e_A^{\hat{p}+}r^p e_B^{\hat{p}-})e^{i\mathbf{K}.(\mathbf{R}-\mathbf{R}')}e^{i\gamma(z+z')} \tag{13}$$

Here K and γ are respectively the parallel and the perpendicular component of the wavevector. r^s and r^p are the Fresnel reflection coefficients for polarisations s and p which depends on the material optical properties and K. Introducing vectors $\hat{s}$ and $\hat{p}^-$ vectors used by Sipe[30] :

$$\hat{s} = \mathbf{K}\times\hat{\mathbf{z}}/K \tag{14}$$

$$\hat{p}^- = \frac{1}{k_0 K}\left[K^2\hat{\mathbf{z}} + \gamma K_x\hat{\mathbf{x}} + \gamma K_y\hat{\mathbf{y}}\right] \tag{15}$$

$$\hat{p}^+ = \frac{1}{k_0 K}\left[K^2\hat{\mathbf{z}} - \gamma K_x\hat{\mathbf{x}} - \gamma K_y\hat{\mathbf{y}}\right] \tag{16}$$

$$\tag{17}$$

one writes the vectors in Green dyadics as

$$e_E^{\hat{s}+} = e_E^{\hat{s}-} = e_H^{\hat{p}+} = e_H^{\hat{p}-} = \hat{s} \tag{18}$$

$$e_E^{\hat{p}+} = -e_H^{\hat{s}+} = -\hat{p}^+ \tag{19}$$

$$e_E^{\hat{p}-} = -e_H^{\hat{s}-} = -\hat{p}^- \tag{20}$$

Moreover, $C_{EE} = \epsilon_0^{-1}$, $C_{EH} = \mu_0 c$, $C_{HE} = \epsilon_0 c$, $C_{HH} = 1$. As already said, when one considers the electromagnetic field at the particle position $\mathbf{r}_p$, only the reflected Green dyadic contributes. In this plane-parallel geometry, $\overleftrightarrow{\mathbf{G}}_R^{EH}(\mathbf{r}_p,\mathbf{r}_p) = \overleftrightarrow{\mathbf{G}}_R^{HE}(\mathbf{r}_p,\mathbf{r}_p) = 0$. Expressions of

the electromagnetic field at the tip position can be obtained from simplification of (5) and (6) taken in $\mathbf{r} = \mathbf{r}_p$. Then

$$\mathbf{E}^{loc}(\mathbf{r}_p) = \left[\overleftrightarrow{\mathbf{I}} - \alpha^E \overleftrightarrow{\mathbf{G}}_R^{EE}(\mathbf{r}_p, \mathbf{r}_p)\right]^{-1} \mathbf{E}^0(\mathbf{r}_p) \tag{21}$$

$$\mathbf{H}^{loc}(\mathbf{r}_p) = \left[\overleftrightarrow{\mathbf{I}} - \alpha^H \overleftrightarrow{\mathbf{G}}_R^{HH}(\mathbf{r}_p, \mathbf{r}_p)\right]^{-1} \mathbf{H}^0(\mathbf{r}_p) \tag{22}$$

leading to the following dipole expressions.

$$\mathbf{p}(\mathbf{r}_p) = \alpha^E \left[\overleftrightarrow{\mathbf{I}} - \alpha^E \overleftrightarrow{\mathbf{G}}_R^{EE}(\mathbf{r}_p, \mathbf{r}_p)\right]^{-1} \mathbf{E}^0(\mathbf{r}_p) \tag{23}$$

$$\mathbf{m}(\mathbf{r}_p) = \alpha^H \left[\overleftrightarrow{\mathbf{I}} - \alpha^H \overleftrightarrow{\mathbf{G}}_R^{HH}(\mathbf{r}_p, \mathbf{r}_p)\right]^{-1} \mathbf{H}^0(\mathbf{r}_p) \tag{24}$$

From these expressions, one notes that dipoles are directly related to the system field in the absence of dipole if one introduces the following effective anisotropic polarisabilities

$$\overleftrightarrow{\alpha}^E = \alpha^E \left[\overleftrightarrow{\mathbf{I}} - \alpha^E \overleftrightarrow{\mathbf{G}}_{EE}^R(\mathbf{r}_t, \mathbf{r}_t)\right]^{-1} \tag{25}$$

and

$$\overleftrightarrow{\alpha}^H = \alpha^H \left[\overleftrightarrow{\mathbf{I}} - \alpha^H \overleftrightarrow{\mathbf{G}}_{HH}^R(\mathbf{r}_t, \mathbf{r}_t)\right]^{-1} \tag{26}$$

that take into account the tip reflexion by the interface. Polarisabilities behavior with the material involved and the tip size and distance to the interface will be studied in the next section.

III. EFFECTIVE POLARISATION BEHAVIOUR

In this section, we consider spherical dipolar particles. In this situation, polarisability values are well established. Note that the polarisability depends, independently from the influence of the interface, on the wavelength and on the ratio of the size particle to the wavelength. We take, in the following, expressions given by Chapuis[31] based on the Mie theory. These expressions apply if the wavelength is much larger than the particle radius R_p. If we introduce $x = \omega R_p/c$ and $y = \sqrt{\epsilon}x$,

$$\alpha_E(\omega) = \epsilon_0 2\pi R_p^3 \frac{2\left[\sin(y) - y\cos(y)\right] - x^2\left[\frac{-\sin(y)}{y^2} + \frac{\cos(y)}{y} + \sin(y)\right]}{\left[\sin(y) - y\cos(y)\right] + x^2\left[\frac{-\sin(y)}{y^2} + \frac{\cos(y)}{y} + \sin(y)\right]} \tag{27}$$

and

$$\alpha_H(\omega) = -2\pi R_p^3 \left[\left(1 - \frac{x^2}{10}\right) + \left(-\frac{3}{y^2} + \frac{3}{y}\cot(y)\right)\left(1 - \frac{x^2}{6}\right)\right] \tag{28}$$

In the next sections, this theory will be mainly applied to the case of Scanning Near-field Microscopy. This is the reason why we choose tungsten particle as tungsten tip are often used in SNOM techniques.

A. Tungsten particle above SiC, SiO2 and Gold

We now study the effective polarisability for two spherical tungsten tip sizes (100nm and 1 μm radii) and above three materials : SiC and SiO2 as dielectrics and gold as a metal.

Let us begin with the case of a 100nm-radius tip of tungsten situated 100 nm above an interface separating vacuum from a material. Note that this corresponds to a sphere that is in contact with the interface. In principle, corrections to the dipolar model should be done since the field is not constant inside the particle so that multipolar contributions are not negligible. This case, used in several SNOM theory can be considered as the limit case of the work presented here. It shows most of the modifications that occur when tip is approached close to a surface.

In the case of a dipolar particle close to a plane interface, 4 different polarisabilities can be identified: parallel electric (α^E_{xx}), perpendicular electric (α^E_{zz}), parallel magnetic (α^H_{xx}) and perpendicular magnetic (α^H_{zz}). They are plotted in Fig. 2.

We note that the electrical perpendicular and parallel polarisabilities are very different from the polarisability of the single particle in vacuum. In particular, we see that a resonance occurs close to the SiC and SiO2 plasmon polariton resonance. This is not surprising since the one interface Green tensors enters in the effective polarisation expression. Since these dyadics, in particular reflection coefficients which enter in their expression, take large values close to frequencies where a resonance is present and at small distance of the interface, the effective polarisability is greatly affected at small distances and close to resonant frequencies. Above gold, no peak is present in the polarisability spectrum since gold does not exhibit resonances in the studied frequency range. Though, polarisability is different from the one in vacuum since the present of evanescent mode close to the interface affect the particle. Inspection of the magnetic polarisation spectra show very different variations the electric one. The main reason for that is that magnetic polarisability in vacuum has different asymptotic variations at small radius r.Two caracteristic lengths enters in the problem : the wavelength λ and the skin depth $\delta = [\Im(\sqrt{\epsilon})k_0]^{-1}$. In the regime where particle radius is small compare

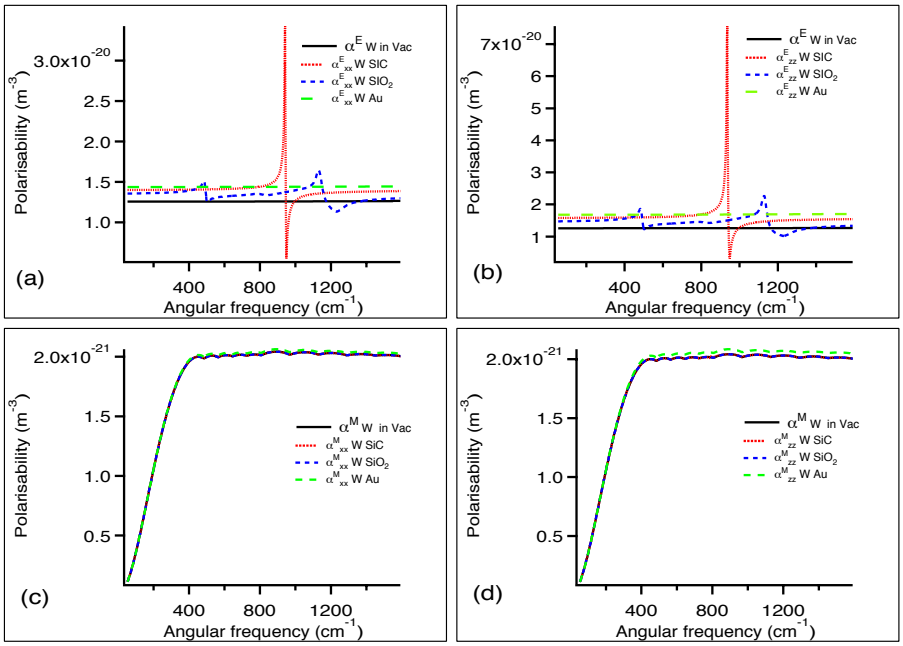

FIG. 2. Parallel electric (a), perpendicular electric (b), parallel magnetic (c) and perpendicular magnetic (d) polarisability for a 100nm-radius spherical tungsten tip situated at z=100 nm above an plane suface of SiC, SiO2 or Gold.

to both λ and δ, vacuum dipolar polarisability behaves as r^3 for electrical polarisability (Clausius-Mossotti limit) and as $r^5 k_0^2$ for the magnetic polarisability[32]. Therefore, if the particle radius is much smaller than the wavelength, magnetic polarisability is smaller so that the correction is smaller. We remark that the correction is larger for gold. This is due to the fact that evanescent magnetic modes are more present above metals than above dielectric due to the metal dielectric constant high values in the infrared. As a consequence, let us finally note that magnetic polarisability is isotropic as corrections are weak.

The same particles polarisabilities have been studied at a larger distance to the interface i.e for 300 nm. The variations are shown in Fig. 3. The electrical polarisabilities spectrum behaviour with variations around resonant frequencies is still present at larger distance although the corrections to the vacuum polarisability are much smaller. This due to the fact that evanescent modes exponentially decay when the distance to the interface increases. This reason also explains why corrections are almost inexistent at z=300 nm for magnetic polarisability.

Let us now study the case of a larger particle (1 μm) situated at 1 μm form the interface.

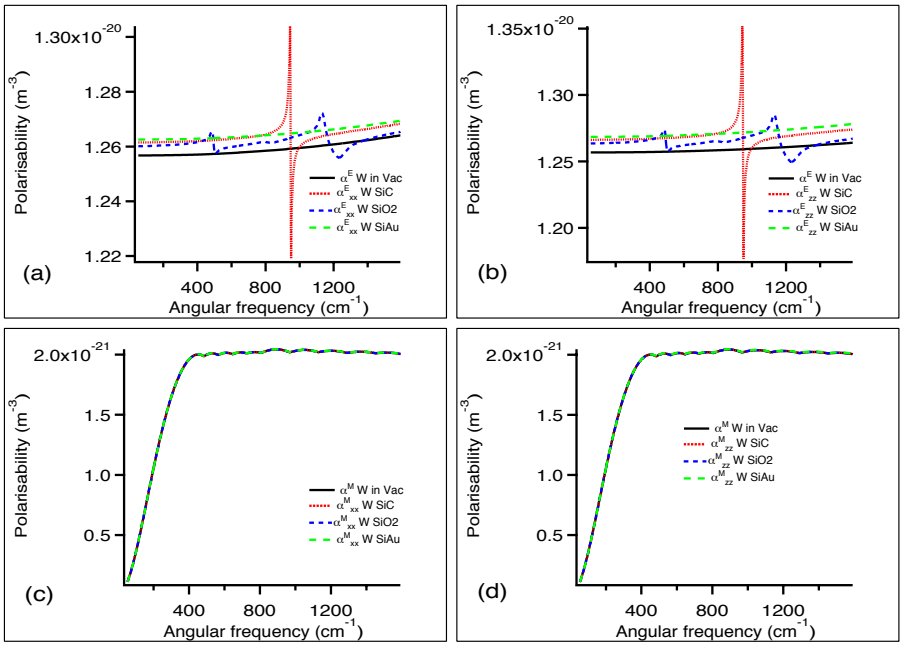

FIG. 3. Parallel electric (a), perpendicular electric (b), parallel magnetic (c) and perpendicular magnetic (d) polarisability for a 100nm-radius spherical tungsten tip situated at z=300 nm above an plane suface of SiC, SiO2 or Gold.

The effective polarisabilities are represented in Fig. 4 . We note important corrections for both electric and magnetic polarisations. These corrections are once again much more important around surface resonance frequencies. The change in the magnetic polarisation is now much more important than for small particles due to the fact that here $k_0 R_p$ is larger. We will see in the next section that retardation effects begin to enter into play at such distances so that corrections at 1μm are different from the one at 100 nm as it can be noticed when one looks carefully at the effective polarisabilities correction curves.

B. Effective polarisability asymptotic expression

We now study the polarisations expression in order to obtain asymptotic expressions for it in some limited physical situations. We first start with Green tensors that appear as an

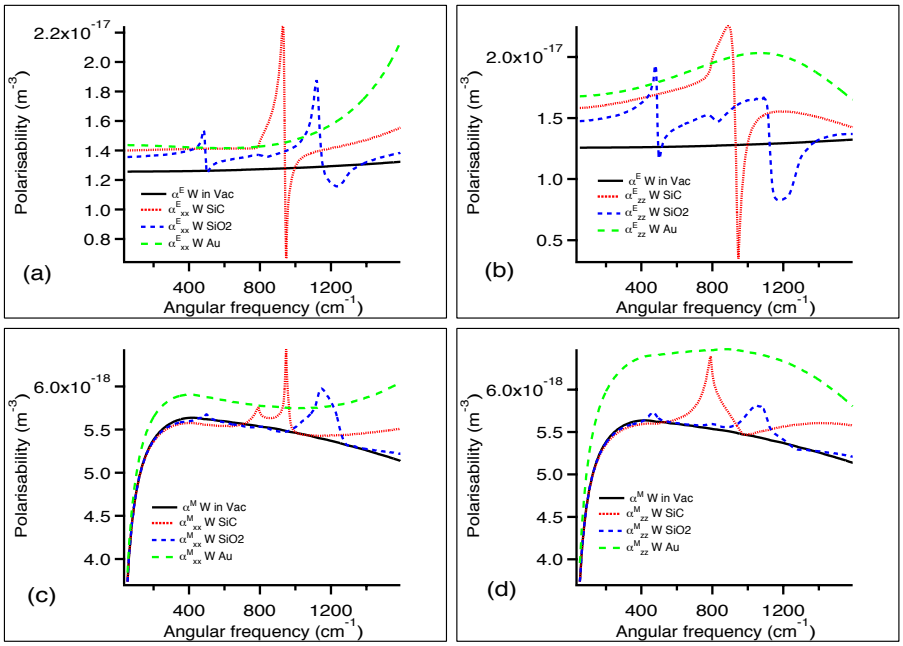

FIG. 4. Parallel electric (a), perpendicular electric (b), parallel magnetic (c) and perpendicular magnetic (d) polarisability for a 1μm-radius spherical tungsten tip situated at z=1 μm above an plane suface of SiC, SiO2 or Gold.

integral over the parallel wavevector :

$$\overleftrightarrow{\mathbf{G}}_R^{EE}(\mathbf{r}_t,\mathbf{r}_t)=\frac{i\mu_0\omega^2}{4\pi}\begin{pmatrix}\int_0^\infty \frac{KdK}{2\gamma}(r^s-r^p\frac{\gamma^2}{k_0^2})e^{2i\gamma z_t} & 0 & 0\\ 0 & \int_0^\infty \frac{KdK}{2\gamma}(r^s-r^p\frac{\gamma^2}{k_0^2})e^{2i\gamma z_t} & 0\\ 0 & 0 & \int_0^\infty \frac{K^3dK}{\gamma k_0^2}r^p e^{2i\gamma z_t}\end{pmatrix} \tag{29}$$

and

$$\overleftrightarrow{\mathbf{G}}_R^{HH}(\mathbf{r}_t,\mathbf{r}_t)=\frac{i\omega^2}{4\pi c^2}\begin{pmatrix}\int_0^\infty \frac{KdK}{2\gamma}(r^p-r^s\frac{\gamma^2}{k_0^2})e^{2i\gamma z_t} & 0 & 0\\ 0 & \int_0^\infty \frac{KdK}{2\gamma}(r^p-r^s\frac{\gamma^2}{k_0^2})e^{2i\gamma z_t} & 0\\ 0 & 0 & \int_0^\infty \frac{K^3dK}{\gamma k_0^2}r^s e^{2i\gamma z_t}\end{pmatrix} \tag{30}$$

We suppose then that the particle is in the dipole approximation and that the separation distance is much larger than the wavelength. In that case, $r^p=(\epsilon-1)/(\epsilon+1)$ and $r^s=(\epsilon-1)k_0^2/4K^2$. Integration over the parallel wavevector is easy since $\gamma^2=k_0^2-K^2\sim -K^2$

so that $\gamma = iK$. Asymptotic expressions of the Green dyadics read

$$\overleftrightarrow{\mathbf{G}}_R^{EE}(\mathbf{r}_t, \mathbf{r}_t) \approx \frac{\mu_0 c^2}{32\pi z_t^3} \begin{pmatrix} \frac{\epsilon-1}{\epsilon+1} & 0 & 0 \\ 0 & \frac{\epsilon-1}{\epsilon+1} & 0 \\ 0 & 0 & 2\frac{\epsilon-1}{\epsilon+1} \end{pmatrix} \tag{31}$$

and

$$\overleftrightarrow{\mathbf{G}}_R^{HH}(\mathbf{r}_t, \mathbf{r}_t) = \frac{k_0^2}{8\pi z_t} \begin{pmatrix} \frac{1}{2}\left(\frac{\epsilon-1}{\epsilon+1} + \frac{\epsilon-1}{4}\right) & 0 & 0 \\ 0 & \frac{1}{2}\left(\frac{\epsilon-1}{\epsilon+1} + \frac{\epsilon-1}{4}\right) & 0 \\ 0 & 0 & \frac{\epsilon-1}{4} \end{pmatrix} \tag{32}$$

So that the effective polarisabilities take the form :

$$\overleftrightarrow{\alpha}^{E} \approx \begin{pmatrix} \frac{\alpha^E}{1-\frac{\alpha^E(\epsilon-1)}{32\epsilon_0\pi z_t^3(\epsilon+1)}} & 0 & 0 \\ 0 & \frac{\alpha^E}{1-\frac{\alpha^E(\epsilon-1)}{32\epsilon_0\pi z_t^3(\epsilon+1)}} & 0 \\ 0 & 0 & \frac{\alpha^E}{1-\frac{\alpha^E(\epsilon-1)}{16\epsilon_0\pi z_t^3(\epsilon+1)}} \end{pmatrix} \tag{33}$$

$$\overleftrightarrow{\alpha}^{H} \approx \begin{pmatrix} \frac{\alpha^H}{1-\frac{\alpha^H k_0^2}{16\pi z_t}\left(\frac{\epsilon-1}{\epsilon+1}+\frac{\epsilon-1}{4}\right)} & 0 & 0 \\ 0 & \frac{\alpha^H}{1-\frac{\alpha^H k_0^2}{16\pi z_t}\left(\frac{\epsilon-1}{\epsilon+1}+\frac{\epsilon-1}{4}\right)} & 0 \\ 0 & 0 & \frac{\alpha^H}{1-\frac{\alpha^H k_0^2}{32\pi z_t}(\epsilon-1)} \end{pmatrix} \tag{34}$$

These expressions are the static limits of the Green-Tensor. This means that no retardation effect is taken into account. Resulting electric polarisation expressions are very close to previous work as done by Knoll and Keilmann[33]. We note in Fig. 5 with the example of a tungsten spherical particle above SiO2 that this approximation is very good for small particles at short distances. For larger particle (1μm particle situated at a 1 μm distance, some deviations exist between exact calculation and asymptotic expressions. This is due to retardation effects that enter into action which are clearly not negligible even at subwavelegth distances as it is presented here. Inspection of Fig. 5 seems to show a similar behaviour for magnetic polarisability i.e. a exact effective magnetic polarisability and static approximation that fit together at short distances and do not fit at large distance. If this feeling is valid at large distance, it is misleading at short distance since corrections to the "naked" magnetic polarisability is small due to polarisability smallness. A fine analysis shows indeed that static approximation is only valid at extremely small distance at the nanometer scale

due to the fact that static limit has a z dependance slower $(1/z)$ than the magnetic one $(1/z^3)$.

IV. APPLICATION TO SNOM DETECTION

The spherical particles which polarisability has been studied in the preceding sections are now used as tips in SNOM experiments. The goal, in this kind of experiment is to study an electromagnetic field close to a surface in the near-field that is at distances much lower than the wavelength considered. The tip scatters the near-field electromagnetic radiation and detects in the far-field at the detector position $\mathbf{r}_d$. The detection scheme is represented in Fig. 6

A. Signal at the detector

We consider here a dipolar tip so that the electromagnetic field at the tip position $\mathbf{r}_t$ create an electric and a magnetic dipole. These dipoles radiate a field which is detected at the detector position in the far field. Thus, the field radiated is just the simple electromagnetic field radiated in far field by an electric and a magnetic dipole taking into account the influence of the interface. The signal at the detector is calculated in the so-called far-field approximation, where the distance has to be large compare to square of scatterer size over the wavelength. The condition is obviously fullfilled here.The signal at the detector can then be considered as a plane wave so that it reads

$$\langle S(\omega)\rangle = \frac{\epsilon_0 c}{2}|\mathbf{E}^d(\omega)|^2 r^2 d\Omega \tag{35}$$

Let us introduce, the elementary vector of the tip-detector direction $\mathbf{u}_d = (\mathbf{r}_d - \mathbf{r}_t)/|\mathbf{r}_d - \mathbf{r}_t| = \mathbf{u}_{d\|} + \mathbf{u}_{d\perp}$ where $\mathbf{u}_{d\perp}$ is perpendicular to the interface. We define $\mathbf{u}_d^- = \mathbf{u}_{d\|} - \mathbf{u}_{d\perp}$, $\hat{s}_d = \mathbf{u}_{d\|} \times \mathbf{e}_z$, $\hat{p}_d^+ = \mathbf{u}_d \times \hat{s}_d$ and $\hat{p}_d^- = -\mathbf{u}_d^- \times \hat{s}_d$. Let us also introduce four more tensors $\overleftrightarrow{\mathbf{h}}(\mathbf{u}_d)$, $\overleftrightarrow{\mathbf{g}}(\mathbf{u}_d)$, $\overleftrightarrow{\mathbf{h}}^R(\mathbf{u}_d)$ and $\overleftrightarrow{\mathbf{g}}^R(\mathbf{u}_d)$.

$$\overleftrightarrow{\mathbf{h}}(\mathbf{u}_d) = \hat{s}_d\hat{s}_d + \hat{p}_d^+\hat{p}_d^+ \tag{36}$$

$$\overleftrightarrow{\mathbf{g}}(\mathbf{u}_d) = -\hat{s}_d\hat{p}_d^+ + \hat{p}_d^+\hat{s}_d \tag{37}$$

$$\overleftrightarrow{\mathbf{h}}^R(\mathbf{u}_d) = (\hat{s}_d r_d^s \hat{s}_d + \hat{p}_d^+ r_d^p \hat{p}_d^-)e^{i\varphi} \tag{38}$$

$$\overleftrightarrow{\mathbf{g}}^R(\mathbf{u}_d) = (-\hat{s}_d r_d^s \hat{p}_d^- + \hat{p}_d^+ r_d^p \hat{s}_d)e^{i\varphi} \tag{39}$$

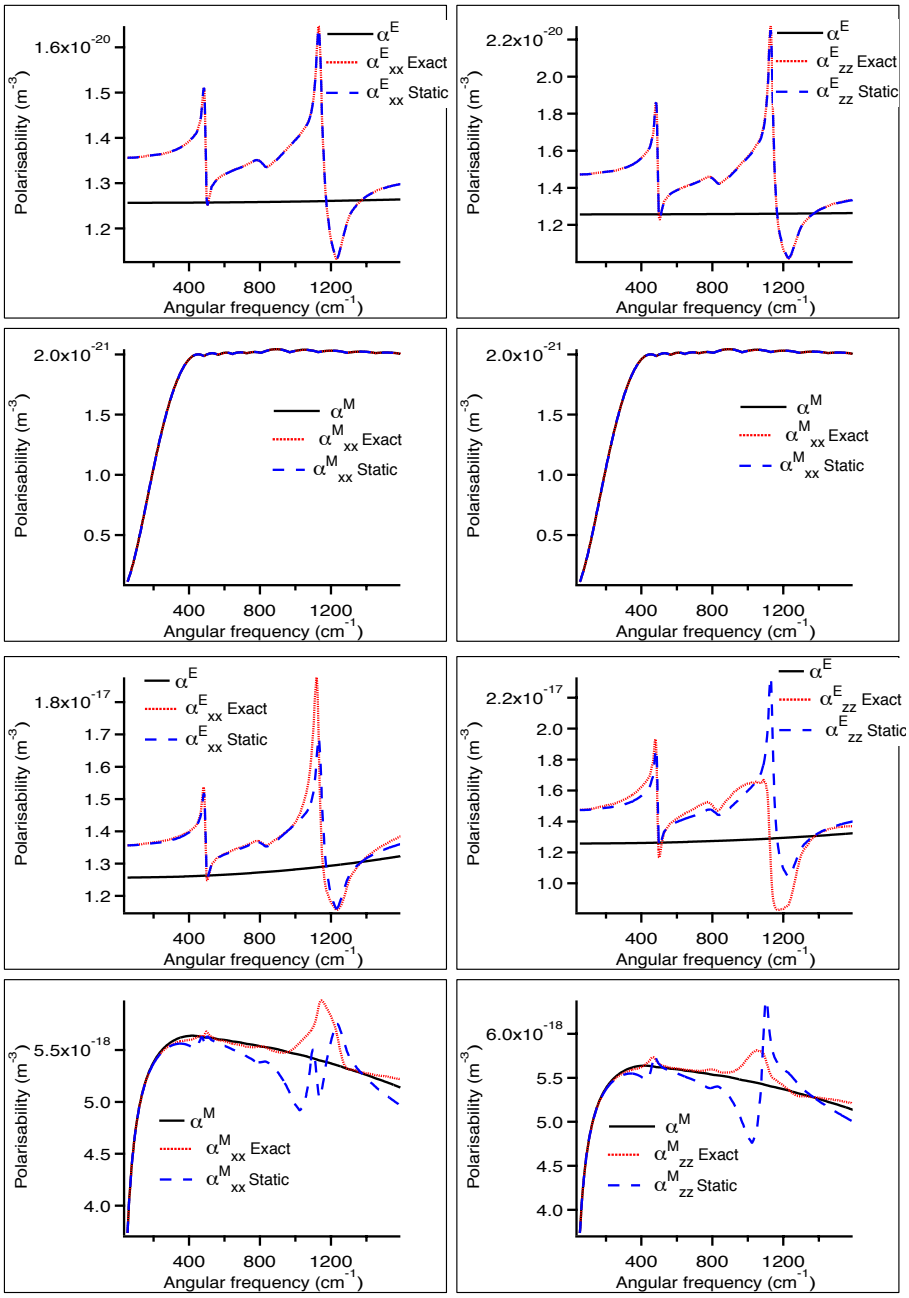

FIG. 5. Comparison between effective polarisabilities obtained with the exact theory developed here and obtained through electrostatic hypothesis. Four top figures : 100nm-radius W sphere situated at $z = 100$ nm of a surface of SiO2. Four bottom figures : 1μm-radius W sphere situated at z=1 μm of a surface of SiO2.

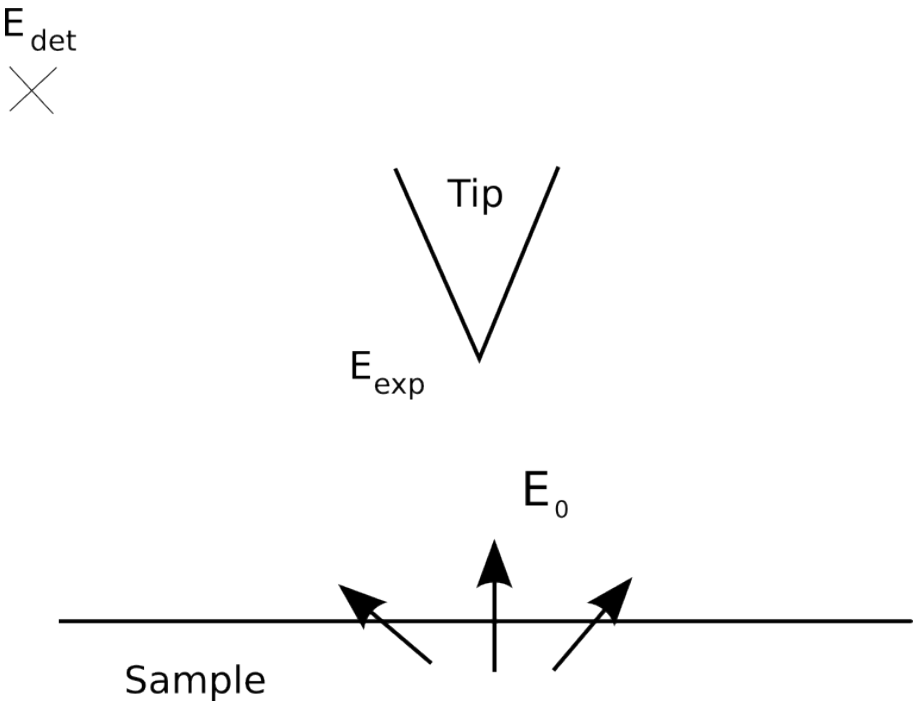

FIG. 6. Detection system scheme

where φ denotes the phase difference between radiation going from tip to the detector and the one going from tip to the detector after one reflection. Following classical expressions of field radiated by dipoles in the far field, the electromagnetic field radiated at the detector is

$$\begin{aligned}\mathbf{E}^d = &\frac{\mu_0\omega^2}{4\pi}\frac{e^{ikR}}{R}\left[\overleftrightarrow{\mathbf{h}}(\mathbf{u}_d)+\overleftrightarrow{\mathbf{h}}^R(\mathbf{u}_d)\right]\overleftrightarrow{\alpha}^E\mathbf{E}^0(\mathbf{r}_t)\\ &+\frac{\mu_0\omega^2}{4\pi c}\frac{e^{ikR}}{R}\left[\overleftrightarrow{\mathbf{g}}(\mathbf{u}_d)+\overleftrightarrow{\mathbf{g}}^R(\mathbf{u}_d)\right]\overleftrightarrow{\alpha}^H\mathbf{H}^0(\mathbf{r}_t)\end{aligned} \tag{40}$$

If we introduce now $\overleftrightarrow{\mathbf{\Gamma}}^E(\mathbf{u}_d)=\overleftrightarrow{\mathbf{h}}(\mathbf{u}_d)+\overleftrightarrow{\mathbf{h}}^R(\mathbf{u}_d)$ and $\overleftrightarrow{\mathbf{\Gamma}}^H(\mathbf{u}_d)=\overleftrightarrow{\mathbf{g}}(\mathbf{u}_d)+\overleftrightarrow{\mathbf{g}}^R(\mathbf{u}_d)$, we find, replacing (35) the expression of the power received at the detector in a solid angle $d\Omega$ around the detector direction:

$$\langle S\rangle = \frac{\mu_0\omega^4 d\Omega}{32\pi^2 c}\sum_{i,j,k}\left(\Gamma^E_{ij}\alpha^E_{jj}E^0_j(\mathbf{r}_t)+\frac{\Gamma^H_{ij}}{c}\alpha^H_{jj}H^0_j(\mathbf{r}_t)\right)\left(\Gamma^{E*}_{ik}\alpha^{E*}_{kk}E^{0*}_k(\mathbf{r}_t)+\frac{\Gamma^{H*}_{ik}}{c}\alpha^{H*}_{kk}H^{0*}_k(\mathbf{r}_t)\right) \tag{41}$$

The final results is a combination of the different electromagnetic field components. These expressions are quadratic expressions of the electromagnetic field component and are related to the electromagnetic energy or the Poynting vector close to the interface.

B. Apertureless SNOM signal detected in some designated situations

1. Expressions of the tensors $\overleftrightarrow{\mathbf{h}}$ *and* $\overleftrightarrow{\mathbf{g}}$.

We consider now a situation where the detector makes an angle θ with the vertical axis in the $z-y$ plane. Therefore, in spherical coordinates, the detector is at position (r_d, φ, θ) with $\varphi = \pi/2$ (Fig. 7). The tip is at position z_t above the interface.

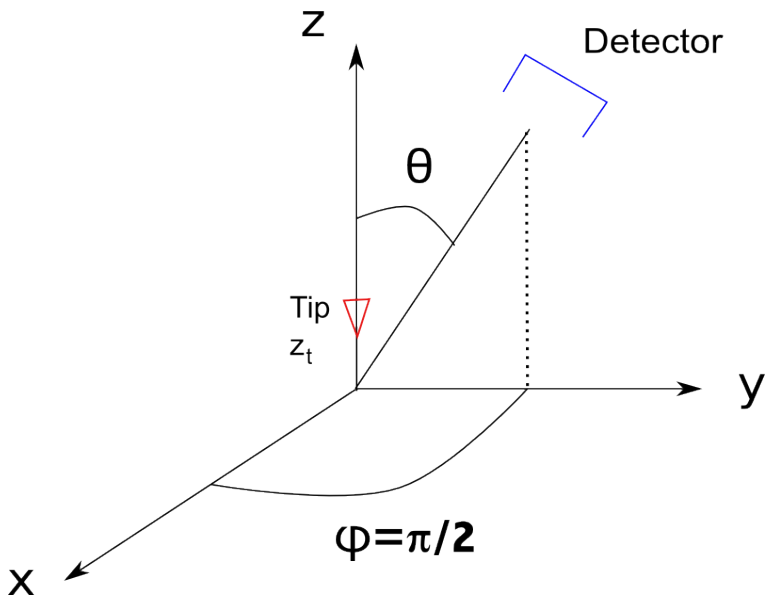

FIG. 7. Tip and detector position

At first order in z_t, the tensors reads

$$\overleftrightarrow{\mathbf{h}}+\overleftrightarrow{\mathbf{h}}^R = \begin{pmatrix} 1+r^s(\theta)e^{2ik_0 z_t\cos\theta} & 0 & 0 \\ 0 & \cos^2\theta(1-r^p(\theta)e^{2ik_0 z_t\cos\theta}) & -\sin\theta\cos\theta(1+r^p(\theta)e^{2ik_0 z_t\cos\theta}) \\ 0 & -\sin\theta\cos\theta(1-r^p(\theta)e^{2ik_0 z_t\cos\theta}) & \sin^2\theta(1+r^p(\theta)e^{2ik_0 z_t\cos\theta}) \end{pmatrix} \tag{42}$$

and

$$\overleftrightarrow{\mathbf{g}}+\overleftrightarrow{\mathbf{g}}^R = \begin{pmatrix} 0 & \cos\theta(1-r^s(\theta)e^{2ik_0 z_t\cos\theta}) & -\sin\theta(1+r^s(\theta)e^{2ik_0 z_t\cos\theta}) \\ -\cos\theta(1+r^p(\theta)e^{2ik_0 z_t\cos\theta}) & 0 & 0 \\ \sin\theta(1+r^p(\theta)e^{2ik_0 z_t\cos\theta}) & 0 & 0 \end{pmatrix} \tag{43}$$

2. Surface Plasmon

We now calculate the signal detected by an apertureless SNOM above a material supporting surface plasmon. Typical materials are metal such as gold and all materials for which the dielectric constant is smaller than -1[34]. Surface plasmon are eigenmode of a plane surface. They correspond to a pole of the plane interface reflexion coefficient. They only exist for TM (or p) polarisation. If z is the vertical direction, the plasmon magnetic field is given by

$$\mathbf{H}(\mathbf{r}) = \left| \begin{array}{c} H_0 e^{i(Ky+\gamma_0 z)} \\ 0 \\ 0 \end{array} \right. \tag{44}$$

whereas the electric field reads from Faraday's law

$$\mathbf{E}(\mathbf{r}) = \left| \begin{array}{c} 0 \\ -\frac{\gamma_0 H_0}{\epsilon\omega} e^{i(Ky+\gamma_0 z)} \\ \frac{K H_0}{\epsilon\omega} e^{i(Ky+\gamma_0 z)} \end{array} \right. \tag{45}$$

If the detector makes an angle θ with the vertical axis and is situated in the $z-y$ plane, the signal at the detector is

$$\begin{aligned} \langle S(\mathbf{r}_d)\rangle = & \frac{\mu_0 c\omega^4}{32\pi^2 c^2}|H_0|^2 e^{-2\Im(K)y} e^{-2\Im(\gamma_0)z} \\ & \times \left[\cos^2\theta |1 - r^p(\theta) e^{2ik_0 z_t \cos\theta}|^2 |\alpha_{xx}^E|^2 \frac{|\gamma_0|^2}{|\epsilon|^2\omega^2} + \sin^2\theta |1 + r^p(\theta)|^2 e^{2ik_0 z_t \cos\theta} |\alpha_{zz}^E|^2 \frac{|K|^2}{|\epsilon|^2\omega^2} \right. \\ & + \frac{|1 + r^p(\theta) e^{2ik_0 z_t \cos\theta}|^2 |\alpha_{xx}^H|^2}{c^2} \\ & + \frac{2\sin\theta\cos\theta}{|\epsilon|^2\omega^2} \Re[(1 - r^p(\theta) e^{2ik_0 z_t \cos\theta})(1 + r^{p*}(\theta) e^{-2ik_0 z_t \cos\theta}) \alpha_{xx}^E \alpha_{xx}^{E*} \gamma_0 K^*] \\ & + \frac{2\cos\theta}{c} \Re\left[(1 - r^p(\theta) e^{2ik_0 z_t \cos\theta})(1 + r^{p*}(\theta) e^{2-ik_0 z_t \cos\theta}) \alpha_{xx}^E \alpha_{xx}^{H*} \frac{\gamma_0}{\epsilon\omega} \right] \\ & \left. + \frac{2\sin\theta}{c} \Re\left[|1 + r^p(\theta) e^{2ik_0 z_t \cos\theta}|^2 \alpha_{zz}^E \alpha_{xx}^{H*} \frac{K}{\epsilon\omega} \right] \right] \end{aligned} \tag{46}$$

In upper Fig. 8, we plot the signal at the detector with the tip-sample distance in the case of a 1 μm-radius tip oscillating in the vertical direction with an amplitude of 150 nm. This conditions are the one use in SNOM experiments such as[17]. We note oscillations when the tip is retracted. This is due to interferences between the signal scaterred by the tip and radiated directly to the detector and the signal scattered by the tip that undergoes a reflection before reaching the detector. The lower Fig. 8 shows the same kind of signal in

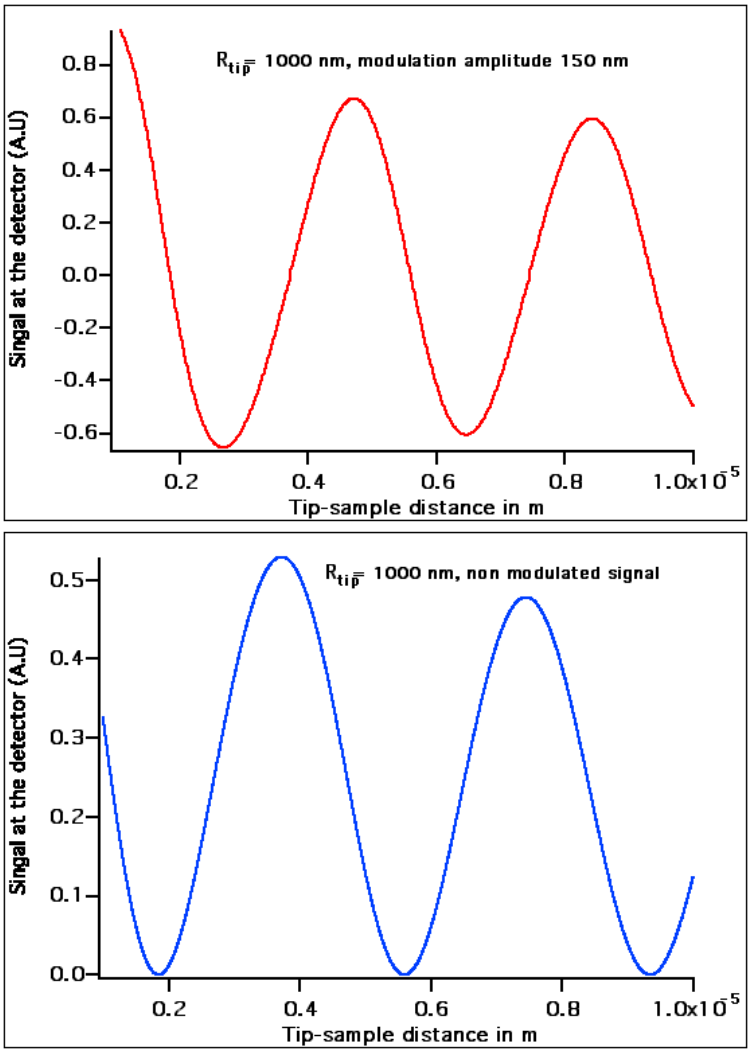

FIG. 8. Theoretical signal above a sample of gold on which a plasmon have been excited for a wavelength $\lambda = 7.5$ μm. Upper figure : signal detected by a 1μm-radius tungsten tip above a gold plane interface supporting a plasmon excited at λ =7.5 μm. The tip oscillates with a 150 nm-amplitude. Lower figure : same conditions as above except that the tip position is not modulated

the case that the tip is not modulated. Signal behaviours obtained from an oscilating tip or an non-oscilating tip are similar. Oscillation period is around $\lambda_{plasmon}/2 = 3.75$ μm and the signal decreases with the tip-sample distance. This is a similar behaviour we observe when on tries to detect plasmonic signal above gold as we can see in Fig. 9. Here the plasmon is excited by a quantum cascade laser at 7.5 μm. Although oscilating period is around 3.75 μm, the signal decays faster than it is theoretically predicted.

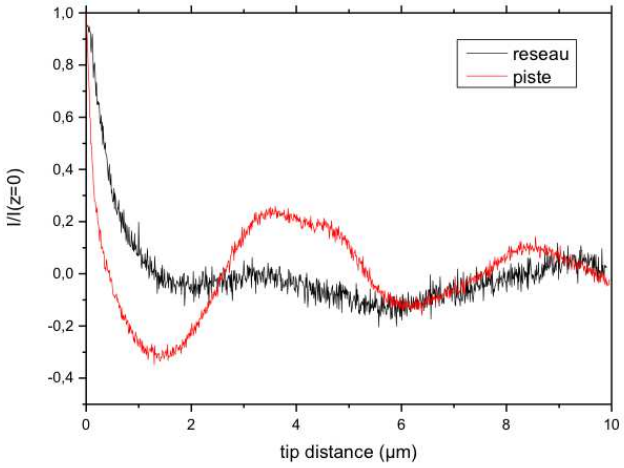

FIG. 9. SNOM signal above a gold sample supporting a plasmon excited by a quantum-cascade laser at 7.5 μm. Detecting tip is made of tungsten and oscilation ampitude is 150 nm.

3. Thermal emission

When the signal above the surface is only the one due to thermal emission, several simplifications occurs. Cross correlations functions such as $\left\langle E_x^0(\mathbf{r}_t)E_y^{0*}(\mathbf{r}_t)\right\rangle$, $\langle E_x^0(\mathbf{r}_t)E_z^{0*}(\mathbf{r}_t)\rangle$, $\left\langle E_y^0(\mathbf{r}_t)E_z^{0*}(\mathbf{r}_t)\right\rangle$, $\left\langle H_x^0(\mathbf{r}_t)H_y^{0*}(\mathbf{r}_t)\right\rangle$, $\langle H_x^0(\mathbf{r}_t)H_z^{0*}(\mathbf{r}_t)\rangle$, $\left\langle H_y^0(\mathbf{r}_t)H_z^{0*}(\mathbf{r}_t)\right\rangle$, $\langle E_x^0(\mathbf{r}_t)H_z^{0*}(\mathbf{r}_t)\rangle$, $\langle E_z^0(\mathbf{r}_t)H_x^{0*}(\mathbf{r}_t)\rangle$, $\left\langle E_y^0(\mathbf{r}_t)H_z^{0*}(\mathbf{r}_t)\right\rangle$ and $\left\langle E_z^0(\mathbf{r}_t)H_y^{0*}(\mathbf{r}_t)\right\rangle$ are all equal to 0 due to the fact that thermal currents are decorrelated for different directions[4]. Moreover, due to rotational symmetry around any axis in the z direction, $\langle|E_x^0(\mathbf{r}_t)|^2\rangle = \left\langle|E_y^0(\mathbf{r}_t)|^2\right\rangle$ and $\langle|H_x^0(\mathbf{r}_t)|^2\rangle = \left\langle|H_y^0(\mathbf{r}_t)|^2\right\rangle$.

In these conditions, the signal at the detector in a direction making an angle θ with the z axis reads

$$\begin{aligned}\langle S(\mathbf{r}_d)\rangle = \frac{\mu_0\omega^4}{32\pi c}d\Omega\Big\{&\left(\cos^2\theta|1-r^p(\theta)e^{2ik_0z_t\cos\theta}|^2+|1+r^s(\theta)e^{2ik_0z_t\cos\theta}|^2\right)|\alpha_{xx}^E|^2|E_x^0(\mathbf{r}_t)|^2\\
&+\sin^2\theta|1+r^pe^{2ik_0z_t\cos\theta}|^2|\alpha_{zz}^E|^2|E_z^0(\mathbf{r}_t)|^2+\frac{\sin^2\theta|1+r^se^{2ik_0z_t\cos\theta}|^2}{c^2}|\alpha_{zz}^E|^2|H_z^0(\mathbf{r}_t)|^2\\
&+\frac{\cos^2\theta|1-r^s(\theta)e^{2ik_0z_t\cos\theta}|^2+|1+r^p(\theta)e^{2ik_0z_t\cos\theta}|^2}{c^2}|\alpha_{xx}^H|^2|H_x^0(\mathbf{r}_t)|^2\\
&+2\cos\theta\Re\Big[\alpha_{xx}^E\alpha_{xx}^{H*}E_x^0(\mathbf{r}_t)H_y^{0*}(\mathbf{r}_t)\\
&\times\left(\frac{(1+r^se^{2ik_0z_t\cos\theta})(1-r^{s*}e^{-2ik_0z_t\cos\theta})+(1-r^pe^{2ik_0z_t\cos\theta})(1+r^{p*}e^{-2ik_0z_t\cos\theta})}{c^2}\right)\Big]\Big\}\end{aligned} \tag{47}$$

Expressions of the electromagnetic field quadratic quantities due to thermal emission above

a plane interface are well known in the literature[4–6] :

$$\left\langle |E_x^0(\mathbf{r}_t)|^2 \right\rangle = \frac{\mu_0 \omega^2 \Theta(\omega,T)}{2\pi^2 c} \Im \left(i \int_0^\infty \frac{udu}{v} \left[1 + r^s e^{2ik_0 vz} + v^2 (1 - r^p e^{2ik_0 vz}) \right] \right) \quad (48)$$

$$\left\langle |E_z^0(\mathbf{r}_t)|^2 \right\rangle = \frac{\mu_0 \omega^2 \Theta(\omega,T)}{\pi^2 c} \Im \left(i \int_0^\infty \frac{u^3 du}{v} (1 + r^p e^{2ik_0 vz}) \right) \quad (49)$$

$$\left\langle |H_x^0(\mathbf{r}_t)|^2 \right\rangle = \frac{\epsilon_0 \omega^2 \Theta(\omega,T)}{2\pi^2 c} \Im \left(i \int_0^\infty \frac{udu}{v} \left[1 + r^p e^{2ik_0 vz} + v^2 (1 - r^s e^{2ik_0 vz}) \right] \right) \quad (50)$$

$$\left\langle |H_z^0(\mathbf{r}_t)|^2 \right\rangle = \frac{\epsilon_0 \omega^2 \Theta(\omega,T)}{\pi^2 c} \Im \left(i \int_0^\infty \frac{u^3 du}{v} (1 + r^s e^{2ik_0 vz}) \right) \quad (51)$$

$$\left\langle E_x^0(\mathbf{r}_t) H_y^{0*}(\mathbf{r}_t) \right\rangle = \frac{\Theta(\omega,T)\omega^2}{4\pi^2 c^2} \left[\int_0^\infty \frac{2uvdu}{|v|} \Re \frac{v}{|v|} (1 + r^s e^{2ik_0 vz} - r^p e^{2ik_0 vz}) \right] \quad (52)$$

where $v = \sqrt{1-u^2}$ and $\Theta(\omega,T) = 1/[\exp[\hbar\omega/(k_b T)] - 1]$ is the mean energy of an oscillator at angular frequency ω at thermal equilibrium. Therefore, if the material and the particle dipole is known, the signal at the detector coming from an emitted thermal electromagnetic field is known. If the signal is divided by the mean energy of an oscillator $\Theta(\omega,T)$, it only depends on the particle polarisability, the tip-sample distance and the surface optical properties. If the polarisability is known, one can wait to map a quantity caracteristic to the surface and to make a surface spectroscopy. Note however that expressions of the effective polarisability and of the thermal electromagnetic field are closely related. Indeed, both are depending of the system Green tensors taken at the tip position. Then, if there is a peak in the quadratic electromagnetic field expressions, there will likely be a peak in the effective polarisability expression. This is a difficulty when one wants to interpret the signal at the detector. Indeed, quadratic electromagnetic quantities are closely related to the electromagnetic LDOS. Relating the signal detector to the LDOS would be very interesting since it would give a way to detect this quantity as electronic tunneling microscopy does it for electronic LDOS[25]. Unfortunately, it is not possible to make a simple relation between the two quantities in general but only in some specific situations.

a. Thermal signal detected above a surface

Case of a polar material We now study the spectrum of the signal detected by a probe above SiC. As we have seen in a previous section, this signal strongly depends on the effective polarisability and therefore of the tip size and the tip distance. To illustrate this point, we now show in Fig. 10 the spectral signal detected by a 100nm probe above SiC and by a 1μm-radius probe. We see that the peak emission is rather narrow for a small tip. This

peak is also situated around the phonon polarition frequency that is 943 cm^{-1} for SiC. We also note that for a small tungsten tip, the signal above SiC is dominated at short distance by electrical terms. We see that both parallel and perpendicular terms have a significant contibution. These contributions though are slighlty shifted : resonance in the effective parallel and perpendicular resonances are indeed different with a factor of 2 difference in the denominator right term leading to a different frequency for the resonant peak.

For a 1 μm tip situated at 1 μm from the interface, we note that the main contribution comes from the parallel electric term. Magnetic terms are also more important here than for small tip due to the fact, as already said, that the magnetic polarisability is larger. Indeed, these magnetic terms do not contribute a lot due to the fact that magnetic energy density is lower than electric energy near the polariton resonance for polar materials. However, the mixed term, which involved both magnetic and electric term is here the second contribution to the signal and is not negligible. in Fig. 10 (c) are presented different spectra of the signal at the detector for spherical tip that would be in contact with the surface. These spectrum are compared with the theoretical spectrum of the LDOS at 100 nm. A 100nm-radius tip gives a signal at the detector similar to the electromagnetic LDOS : a strong peak appears around the polariton frequency. If the peak width is very close to the LDOS one, the peak position is nevertheless slightly shifted. When the tip size increases, the peak observed for small tip at short distances is shifted and broadened. Recent SNOM experiment seems to show this shifiting and broadening suggesting that tips behaves like micrometric spherical tips. Note also that this broadening although less pronounced than for a large tip, also occurs when a small tip is retracted from the surface as it can be seen in Fig. 10 (d).

b. What is detected at the detector? As shown in Fig. 10, signal obtained with small tip is very similar to the LDOS signal around the polariton resonance. At short distance, the signal is indeed mainly dominated by the parrallel electric contribution. This means that the signal mainly depends on α_{xx}^{E} and on $|E_x^0|^2$. In the case of a thermal signal, this last quantity is representative of the electrical energy density and of the electromagnetic LDOS. Therefore, a SNOM experiment detecting near-field thermal field, will be a product of the effective polarisability and of a partial contribution to the LDOS. If effective polarisability has a flat response i.e. its variations are small with the frequency, one can say that the signal at the detector is proportionnal to the LDOS. This is not the case in the present situation where polarisability can be increased by a factor of 3 to 5 around the resonance : the

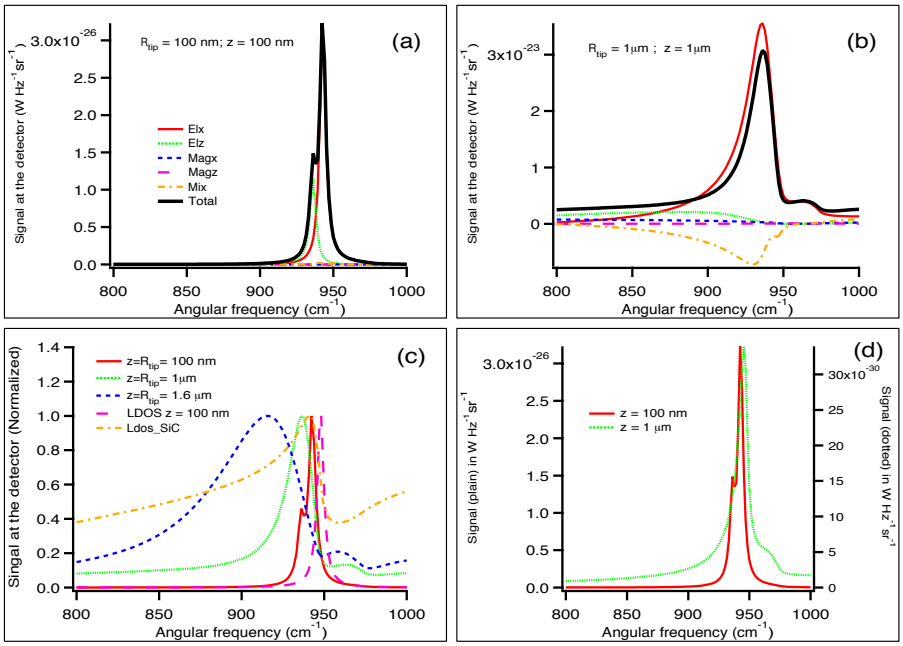

FIG. 10. Signal spectrum at the detector. The tip is constituted of a W spherical particle situated above SiC. The signal is detected in a direction making an angle of 30^0 with the vertical (a) Total signal and different contributions for a 100nm radius tip at z =100nm above surface. (b) Total signal and different contributions for a 1 μm radius tip at z =1 μm above surface. (c) Signal spectrum for $z = R_{tip} = 100$ nm, $z = R_{tip} = 1$ μm and $z = R_{tip} = 1.6$ μm. Comparison with LDOS (d) Signal spectrum for $R_{tip} = 100$ nm and two different distances to the interface $z = 100$ nm and $z = 1.6$ μm.

resulting signal is the product of two peaks situated approximately at the same frequency. As LDOS in the peak spectral band is 100 to 1000 times LDOS outside this band, its multiplication by effective polarisability will give a peak that is not exactly the LDOS but which is representative of the LDOS

We now consider larger tips of micrometer size radii. The signal at the detector scattered by such tips has a broader spectrum and the frequency corresponding to the emission spectrum is shifted to the lower frequencies i.e. the higher wavelength. When one the tip size increases, polarisability is shifted to lower frequency and broadened. A higher distances, LDOS is also broadened and shifted but differently than polarisability. Frequecy shift is indeed less important for LDOS. The resulting signal is now the product of two peaks which are rather similar in terms of broadness but with their maxima separated. The resulting

signal is a peak situated between the polarisability and LDOS peaks. In these conditions, the signal at the detector is a peak related to the LDOS but which is not stricly speaking the LDOS

Note that this situation can be observed experimentally above Quartz.

c. Case of a metal We now consider the example of a tip situated above a metal surface. In Fig. 11 is represented the signal scattered by a tungsten particle above a gold surface heated at 300 K. In the case of a small particle, the contribution to the signal is dominated by the magnetic term below 1000 cm^{-1}. The main reason for that is due to the fact that magnetic energy is more important than electrical energy in this part of the spectrum where Au is highly reflecting. As seen in Fig. 2 magnetic polarisability has a flat response for small tips above 400 cm^{-1}. Then, between 400 and 1000 cm^{-1} the signal at the detector is proportional to parallel magnetic energy which is close to total electromagnetic energy. Thus, the signal detector in this spectral range is close to the LDOS. Above 1000 cm^{-1} on the contrary, the signal is dominated by the perpendicular electric contribution although parallel magnetic and the mixed term are lower but of the same order of magnitude than the dominant term. In this kind of situation, it becames difficult to say that the signal is proportional to the LDOS although it is related to it. For a large tip, there is no spectral range where a term dominates the contribution to the signal except at high frequency where the dipole approximation has its validity that become questionable. Therefore, it is hard to relate the signal to the LDOS in this situation.

V. RADIATIVE COOLING OF A DIPOLAR PARTICLE

When a dipolar particle is heated, one can calculate the rate at which it will exchange energy with the outside. The spectral power lost by a particle at temperature T with vacuum at null temperature is[35]

$$P(\omega)d\omega = \frac{\omega^3}{\pi^2 c^3} Im[\alpha(\omega)]\Theta(\omega, T)d\omega \tag{53}$$

When the particle is close to a surface, it has been shown in the past that the particle exchanges with the surface with a dependance of the polarisability and of the electromagnetic energy density at the particle position. This phenomenon is very similar to the Purcell effect when an atom or a molecule has its spontaneaous emission rate that is modified when

approached close to a surface. The cooling rate depends on the electromagnetic LDOS in a similar way spontaneous emission rate depends on the LDOS[36]. The cooling rate formula given in the paper of Mulet et al.[26] should be corrected. Indeed, the interaction of the particle with the surface should be taken into account through the effective polarisability. The formula of the cooling rate of a particle placed close to a sample at null temperature reads

$$P(\omega)d\omega = \frac{2}{\pi}\frac{\omega^2}{c^2}\Theta(\omega,T)\sum_{i=x,y,z}\Im(\alpha_{ii}^E)\Im\left[G_{ii}^{EE}(\mathbf{r}_p,\mathbf{r}_p)\right]d\omega \tag{54}$$

We plot in Fig. 12, the heat exchanged at 300 K with the distance and the spectrum of the heat exchanged between a 100nm radius SiC particle above a SiC substrate at zero temperature. We compare, in each plot, expression presented in this paper and the one obtained by Mulet[26]. In the power exchanged curve versus particle interface distance, we note that both expression gives similar results to distances as low as 400 nm. At large distances, corrections to the polarisability are small and electromagnetic field is mainly dominated by propagative wave contributions. Heat exchanged is spectrally dominated by the region where a resonance occurs in the SiC particule around 935 cm^{-1} i.e. where $\epsilon = -2$. When one enters in the near field, two phenomena occur : electromagnetic field is dominated by evanescent contributions, in particular those coming from the phonon polariton resonance occuring next to the frequency where ϵ=-1. Moreover, when the particle interface disctance is reduced, corrections to the polarisability appear. In the present case, particle resonance peak is weakened what explained the fact that at 100 nm, exact expression of the transfer gives a lower contribution than the one used by Mulet et al.

VI. THERMAL EMISSION OF A NANOPARTICLE

We now consider a small dipolar particle heated at temperature T. This particle radiates an electromagnetic field in all space. This field is a thermal field which is here detected in far-field by a detector. The signal at the detector has a contribution coming directly from the particle in straight line or after one reflection at the interface. The signal at the detector has the following expression:

$$\langle S(\omega)\rangle = \frac{d\Omega}{32\pi^3}\Theta(\omega,T)\frac{\omega^3}{c^3}\left[\Im[\alpha_{xx}^E]\left(|1+r^s(\theta)e^{2ik_0z_t\cos\theta}|^2+\cos^2\theta|1-r^p(\theta)e^{2ik_0z_t\cos\theta}|^2\right)\right.$$

$$+ \Im[\alpha_{zz}^{E}]|1 + r^{p}(\theta)e^{2ik_0 z_t \cos\theta}|^2 \sin^2\theta\Big] \tag{55}$$

In this expression, the spectral dependance comes mainly from the effective polarisability and also from the far field reflection coefficient. One thus waits that the spectral signal detected will follow polarisability variations that we have described in the preceding sections.

In Fig. 13, we plot the signal detected in far field by a detector in the 45^0 direction from the vertical direction in the case of a 100 nm-radius tungsten spherical particle heated at 300 K situated at different distances from the interface separating vacuum from SiC. When particle-interface distance is 100 nm, the signal is peaked around SiC plasmon resonance, as is 100 nm-radius tungsten spherical particle polarisability. When the particle is retracted from the interface, the signal is reduced and widens. Above a certain distance, effective polarisability is nothing but the polarisability in vacuum. For tungsten, this polarisability has a rather flat dependance with the frequency. Signal spectral behaviour mainly comes refelction coefficient spectral variations. One notes that the signal is more important in the frequency range where SiC is known to be highly reflective i.e. between $1.6\times\ 10^{14}$ rad s^{-1} and $1.8\times\ 10^{14}$ rad s^{-1} . Similar behaviour is observed for a micrometric tip except that the signal is broader at the minimum distance. This can easily be explained by inspecting effective polarisability of a 1 μm-radius spherical tungsten tip situated at 1 μm of a SiC interface where the noticed broadening is indeed observed.

Note that in this kind of situation, the signal at the detector can exhibit a peak very similar to the one observed near SiC in the energy density spectrum that is in the electromagnetic LDOS. However, this peak is the signature of the effective polarisability which exhibit resonance at frequencies close to surface resonance. If experiments done in the present situations do not probe electromagnetic LDOS, we see that if the tip is sufficiently close to the interface, it can probe surface resonance. It can then also be seen as a surface spectroscopy method.

VII. CONCLUSION

We have seen in this article, how a dipolar particle has its polarisability that is modified when its distance to the interface is reduced. Multiple reflections between the tip and the interface modify the polarisability through the interface Green tensor. When a dipolar tip is used to detect the near-field infrared thermal electromagnetic field close to a heated material

(TRSTM experiment), the signal depends on both effective polarisability and electromagnetic energy density. These two quantities, as well as the electromagnetic LDOS depends on the interface Green function so that the signal at the detector in a TRSTM experiment can be strongly related to the electromagnetic LDOS. As LDOS modifies molecular desexcitation rate, it also modifies thermal cooling of a particle close to a surface. Moreover, particle effective polarization plays a role in the thermal cooling process. At last, we have shown that making the spectrum in far field of the thermal field emitted by a dipolar particle at a subwavelength distance of an interface could be used to perform a material spectroscopy.

ACKNOWLEDGMENTS

The authors thanks Jean-Jacques Greffet for fruitful discussions. K.Joulain, Y. De Wilde and P. Ben-Abdallah thank ANR contracts NANOFTIR 07-NANO-039 and SOURCES-TPV BLAN-0928-01 for financial supports. Y. De Wilde and Arthur Babuty thank CNANO IDF for PhD grant financial support.

---

[1]

[2] 08, 1.

[3] S.M. Rytov, Y.A. Kravtsov, and V.T. Tatarskii. *Principle of Statistical Radiophysics 3*, volume 3 of *Elements of Radiation Fields*. Springer Verlag, 1989.

[4] Karl Joulain, Jean-Philippe Mulet, François Marquier, Rémi Carminati, and Jean-Jacques Greffet. Surface electromagnetic waves thermally excited: Radiative heat transfer, coherence properties and Casimir forces revisited in the near field. *Surface Science Reports*, 57(3-4):59–112, May 2005.

[5] A Volokitin and B Persson. Near-field radiative heat transfer and noncontact friction. *Reviews of Modern Physics*, 79(4):1291–1329, October 2007.

[6] I A Dorofeyev and E A Vinogradov. Fluctuating electromagnetic fields of solids. *Physics Reports*, 504(2-4):75–143, July 2011.

[7] D Polder and M. van Hove. Theory of Radiative Heat Transfer between Closely Spaced Bodies . *Physical Review B*, 4:3303–3314, November 1971.

[8] A.V. Shchegrov, K Joulain, R Carminati, and J J Greffet. Near-field Spectral Effects due to Electromagnetic Surface Excitations. *Physical Review Letters*, 85:1548–1551, August 2000.

[9] C Henkel, K Joulain, R Carminati, and J J Greffet. Spatial Coherence of thermal near-fields. *Optics Communications*, 186:57–67, December 2000.

[10] Jean-Jacques Greffet, Rémi Carminati, Karl Joulain, Jean-Philippe Mulet, Stéphane Mainguy, and Yong Chen. Coherent emission of light by thermal sources. *Nature*, 416:61–63, March 2002.

[11] B.J. Lee and Z M Zhang. Design and fabrication of planar multilayer structures with coherent thermal emission characteristics. *Journal of Applied Physics*, 100:063529, September 2006.

[12] Gabriel Biener, Nir Dahan, Vladimir Kleiner, and Erez Hasman. Highly coherent thermal emission obtained by plasmonic bandgap structures. *Applied Physics Letters*, 92:081913, February 2008.

[13] Achim Kittel, Wolfgang Müller-Hirsch, Jürgen Parisi, Svend-Age Biehs, Daniel Reddig, and Martin Holthaus. Near-Field Heat Transfer in a Scanning Thermal Microscope. *Physical Review Letters*, 95(22), November 2005.

[14] Arvind Narayanaswamy, Sheng Shen, and Gang Chen. Near-field radiative heat transfer between a sphere and a substrate. *Physical Review B*, 78(11), September 2008.

[15] Emmanuel Rousseau, Alessandro Siria, Guillaume Jourdan, Sebastian Volz, Fabio Comin, Joël Chevrier, and Jean-Jacques Greffet. Radiative heat transfer at the nanoscale. *Nature Photonics*, 3:514–517, August 2009.

[16] R Ottens, V Quetschke, Stacy Wise, A Alemi, R Lundock, G Mueller, D Reitze, D Tanner, and B Whiting. Near-Field Radiative Heat Transfer between Macroscopic Planar Surfaces. *Physical Review Letters*, 107(1), June 2011.

[17] Yannick De Wilde, Florian Formanek, Rémi Carminati, Boris Gralak, Paul-Arthur Lemoine, Karl Joulain, Jean-Philippe Mulet, Yong Chen, and Jean-Jacques Greffet. Thermal radiation scanning tunnelling microscopy. *Nature*, 444(7120):740–743, December 2006.

[18] Yusuke Kajihara, Keishi Kosaka, and Susumu Komiyama. Thermally excited near-field radiation and far-field interference. *Optics Express*, 19:7695–7704, April 2011.

[19] F J García de Abajo. Colloquium: Light scattering by particle and hole arrays. *Reviews of Modern Physics*, 79(4):1267–1290, October 2007.

[20] F Intravaia, C Henkel, and M Antezza. Fluctuation-induced forces between atoms and surfaces: the Casimir-Polder interaction. In D Dalvit, P Milonni, D Roberts, and F da Rosa, editors,

Lecture Notes in Physics, pages 345–391. arXiv.org, October 2010.

[21] Philippe Ben-Abdallah, Svend-Age Biehs, and Karl Joulain. Many-Body Radiative Heat Transfer Theory. *Physical Review Letters*, 107(11), September 2011.

[22] Étienne Castanié, Rémi Vincent, Romain Pierrat, and Rémi Carminati. Absorption by an optical dipole antenna in a structured environment. *arXiv.org*, November 2011.

[23] Karl Joulain, Rémi Carminati, Jean-Philippe Mulet, and Jean-Jacques Greffet. Definition and measurement of the local density of electromagnetic states close to an interface. *Physical Review B*, 68(24), December 2003.

[24] A Kittel, U F Wischnath, J Welker, O Huth, F Rüting, and S A Biehs. Near-field thermal imaging of nanostructured surfaces. *Applied Physics Letters*, 93(19):193109, 2008.

[25] J. Tersoff and D.R. Hamann. Theory of the scanning tunneling microscope. *Physical Review B*, 31(2):805–813, January 1985.

[26] Jean-Philippe Mulet, Karl Joulain, Rémi Carminati, and Jean-Jacques Greffet. Nanoscale radiative heat transfer between a small particle and a plane surface. *Applied Physics Letters*, 78:2931–2933, May 2001.

[27] Karl Joulain and Jérémie Drevillon. Noncontact heat transfer between two metamaterials. *Physical Review B*, 81(16), April 2010.

[28] Melvin Lax. Multiple Scattering of Waves. *Reviews of Modern Physics*, 23:287–310, October 1951.

[29] Philippe Ben-Abdallah and Karl Joulain. Fundamental limits for noncontact transfers between two bodies. *Physical Review B*, 82(12), September 2010.

[30] J.E. Sipe. New Green-functions formalism for surface optics. *J. Opt. Soc. Am B*, 4:481–489, April 1987.

[31] Pierre-Olivier Chapuis, Sebastian Volz, Carsten Henkel, Karl Joulain, and Jean-Jacques Greffet. Effects of spatial dispersion in near-field radiative heat transfer between two parallel metallic surfaces. *Physical Review B*, 77(3), January 2008.

[32] Pierre-Olivier Chapuis, Marine Laroche, Sebastian Volz, and Jean-Jacques Greffet. Radiative heat transfer between metallic nanoparticles. *Applied Physics Letters*, 92(20):201906, 2008.

[33] Bernhardt Knoll and Fritz Keilmann. Enhanced dielectric contrast in scattering-type near-field optical microscopy. *Optics Communications*, 182:321–328, August 2000.

[34] Heinz Raether. *Surface Plasmons on Smooth and Rough Surfaces and on Gratings*, volume 111 of *Springer Tracts in Modern Physics*. Springer-Verlag, Berlin, 1988.

[35] Karl Joulain. Radiative Transfer on Short Length Scales. *Topics in Applied Physics*, 107:107–131, March 2008.

[36] P Ben Abdallah, F.S.S. Rosa, M. Tschikin, and S A Biehs. Radiative cooling of nanoparticles close to a surface. *arXiv.org*, December 2011.

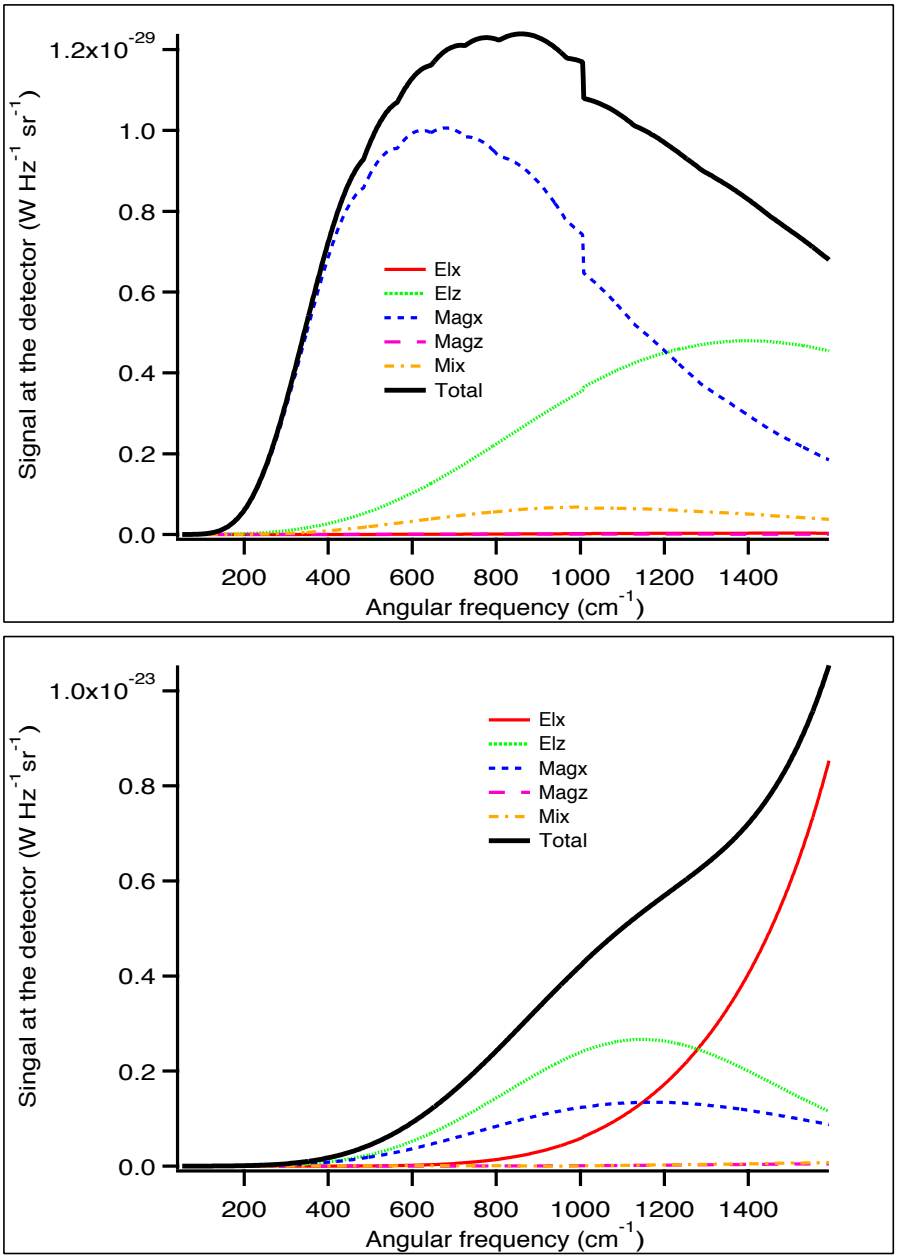

FIG. 11. Signal spectrum at the detector. The tip is constituted of a W spherical particle situated above Au. The signal is detected in a direction making an angle of 30^0 with the vertical (upper) Total signal and different contributions for a 100nm radius tip at z =100nm above surface. (Lower) Total signal and different contributions for a 1 μm radius tip at z =1 μm above surface.

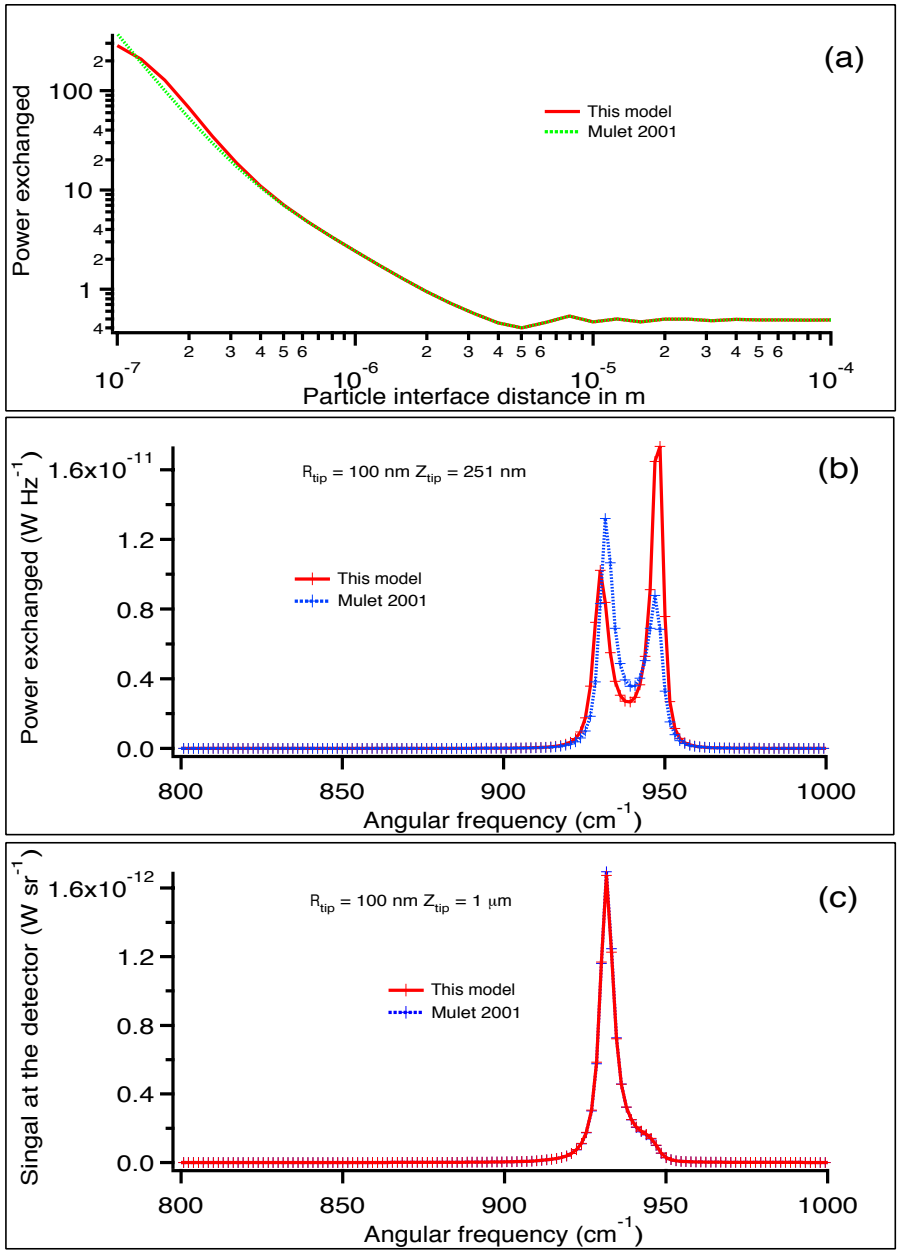

FIG. 12. (a) Heat transfer between a 100nm radius SiC particle at 300 K above a SIC substrate at null temperature versus distance. (b) Power exchanged spectrum between a 100 nm radius SiC particle above a SiC substrate at zero temperature situated at 251 nm below the particle. (c) Power exchanged spectrum between a 100 nm radius SiC particle above a SiC substrate at zero temperature situated at 1 μm below the particle.

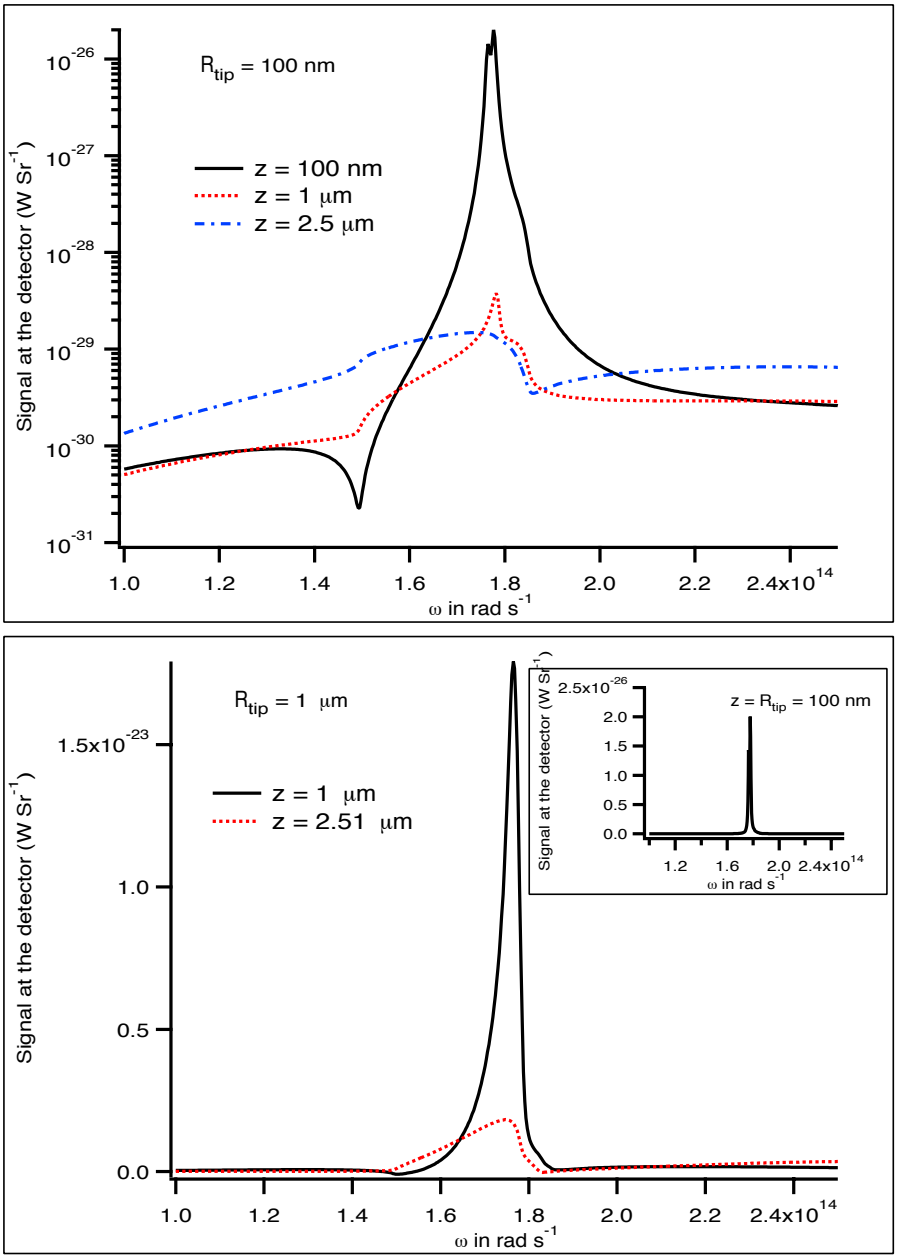

FIG. 13. Signal at the detector which direction makes an angle $\theta = 45^0 C$ with the vertical axis. The tip is a spherical tip of tungsten heated at $T = 300$ K and situated at various particle-SiC interface. Upper figure : signal in log-scale for R_{tip}= 100 nm and for three different tip-sample distance. Lower figure : signal in linear scale for R_{tip}= 1 μm and for separation distance equal to 1 μm and 2.51 μm. Inset : signal for $z = R_{tip}$= 100 nm.